Journal of Sol-Gel Science and Technology 11, 217–227 (1998)

Structure of CdS/SiO_2 Nanocomposites: Influence of the Precursor and Cd Concentration

LUIS ESQUIVIAS, ROCÍO LITRÁN, JULIÁN RODRÍGUEZ-ORTEGA, EDUARDO BLANCO, MILAGROSA RAMÍREZ-DEL-SOLAR AND NICOLÁS DE LA ROSA-FOX
Departamento de Física de la Materia Condensada, Facultad de Ciencias, Universidad de Cádiz, Apartado 40, Puerto Real, 11517 Cádiz, Spain

Received March 26, 1997; Accepted December 22, 1997

Abstract. The influence of using TMOS or TEOS in the formation of CdS quantum dots in a silica matrix have been studied by X-ray absorption spectroscopy (XAS). The amount of Cd─S bonds have been monitored as a function of the nominal Cd concentration. The relative amount of CdS crystals depends on the precursor. The use of TEOS is not recommended because it gives a poor yield, especially for high Cd concentration. A discussion of the influence of CdS concentration in matrices from TMOS is carried out from structural models created from their pore volume distribution. The mean pore size becomes smaller and the size distribution more uniform when CdS concentration increases but the nanocrystals of low CdS nominal content present a more efficient quantum confinement.

Keywords: quantum dots, nanocomposites, XAS, structure model

1. Introduction

Ten or fifteen years ago, when the major of the sol-gel research was obtaining bulk unusual glasses, the difficult elimination of the gel pores was one of the main drawbacks of the process. Nowadays, the attention of many researchers is focused on nanocomposites, membranes and catalyst, and, curiously, the main interest of the sol-gel route results from their porous structure. In the field of nanocomposite, the discovery of Jain and Lind [1], that glasses containing semiconductor crystallites, present optical nonlinearity, investigations were headed toward the processing of these type of materials. Typical systems are constituted by glasses containing crystallites of a chalcogenide of a heavy metal. Xerogels are adequate to grow small crystals exhibiting quantum-confinement behavior because the high reactivity of the pores permits to use them as host matrices for chemical reactions [2]. Sono-xerogels are potentially better candidates because these materials are not hygroscopic and do not present ageing effect even after being examined with high power laser beams [3].

In many cases, cation is previously embedded in the matrix, by adding a salt to the precursor sol. In a second step, the semiconductor particles are formed when the doped gel is exposed to the diffusion of some liquid or gaseous compound of the chalcogenide through the porous network [4, 5]. In a second approach, the cation salt reacts with some sulphide precursor, as thiourea, in the precursor sol. This reaction leads to the formation of a complex, trapped in the pores, which can be transformed into sulphide upon heat treatment [6, 7]. Although sulphide particles can be obtained in the quantum regime, these methods do not allow particle growth and stabilization process independent of the incorporation to the matrix. Alternative strategies for the control of particle size and size distribution have been found in the classical colloidal chemistry. The basic idea is to incorporate semiconductor quantum dots (Q-particles) to the gel by the addition of the gel precursor to a stable colloid [8]. Schmidt's group has reported several works [9–12] based on the preparation of semiconductor or metal Q-particles in the presence of a functionalized alkoxide. By this method a

semiconductor precursor is formed in which the clusters are carrying multifunctional polymerizable ligands that will be transformed to nanocomposite by reaction. Consequently, growth and agglomeration of the particles are inhibited by stabilization and surface modification.

In the case that all or part of the components is introduced by diffusion methods, the reaction depends on the size and geometry of the pores. Popular choices used in the preparation of silica-based gels are tetramethoxysilane, $Si(OCH_3)_4$, and tetraethoxysilane, $Si(OC_2H_5)_4$, known as TMOS and TEOS, respectively. Choosing between them might not be a trivial matter because the precursor strongly affects the texture but no studies have been done. However, curiously, relevant papers from the early years of this research present only results on nanocomposite materials in which the silica-based matrix have been prepared from TEOS [13–16]. Likewise, in the case of metal oxides/ormosils nanocomposite TEOS was used for inorganic precursor of the hybrid gel [17].

Sonogels [18, 19] obtained exposing the initial TEOS-water mixture to intense ultrasounds radiation, present enhanced small and uniform size pores and high mechanical resistance [20–22]. Although sonogels are prepared under acid catalyst, they present structure features different from classic gels prepared in acidic conditions [23]. The same as basic catalyst, ultrasounds promote hydrolysis [24] resulting in a particulate structure. This notable characteristic is induced both the solventless processing and the cavitation phenomenon, responsible for the alkoxide-water mixture homogenization. The pore-size distributions in dried sonogels turn out to be influenced by the presence of DCCA (Drying Control Chemical Additive) [25, 26]. Those prepared with formamide have a very narrow distribution and this radius is smaller than 2 nm—less than a half of hypercritically dried sonogels. They have been tested to prepare these materials as these characteristics were considered that would magnify the potential feasibility of the sol-gel processing of composites [27]. Bagnall and Zarzycki obtained CdS_xSe_{1-x} nanocrystal in sonogel matrices prepared with DCCA [28] by chemical reaction in the interstitial liquid. They found that the smaller diffusivity in sonogels, as compared to classic wet gels, enabled fine and uniform nanocrystals to be obtained.

When the cation is introduced into the sol prior to gelation, its concentration influences the porous texture [29]. There is a combined effect cation- precursor that is unknown at what extent affects the diffusion of the missing component from external sources. This work presents an attempt to elucidate the influence of the matrix precursor on the formation of CdS quantum dots in a silica matrix. Certainly, the densification of the gel/CdS nanocomposite is required to stabilize the system, representing the main drawback of this processing. The problem is to keep a crystallite size small enough to show quantum confinement, knowing that the exciton Böhr radius is 30 Å for CdS. We have shown, following the method proposed by Yamane et al. [30], that heat treatment (400–500°C) of the samples before H_2S diffusion in order to oxidize the cadmium of the doped gel is enough to guarantee a high efficiency in the conversion to CdS [31]. In this way, sulphidation at 200°C leads to CdS particles formation by a solid-state reaction. The final composites resulting after heating (∼500°C) under inert atmosphere are very stable and contain good quality CdS particles.

X-ray absorption spectroscopy (XAS) allows the structural characterization around a localized atomic specie, even in the case that it was very diluted. Because of its selectivity, if the short-range orders of the involved species are different enough, it can be use to study the homogeneity of the material at an atomic level. On the other hand, in a former paper [32], we described the structure of xerogels prepared with DCCA as successive levels assemblies of close packed spheres of radius R_{i+1} following the approach initiated by Zarzycki [33, 34]. In this paper we have applied our models to correlate the composite structure with XAS conclusions.

2. Experimental

2.1. Composite Preparation

Silica sono-xerogels were prepared by ultrasonically assisted hydrolysis of a mixture of TMOS or TEOS : acidic water : formamide in the molar ratio 1 : 10 : 3 using an ultrasonic dose of 0.064 J/L. Different amounts of $Cd(NO_3)_2$ were added under mechanical agitation to the sono-solutions before gelation. Once the resulting gels aged and dried at room temperature, CdS particles were formed by H_2S gas difussion through cadmium doped xerogels at 200°C. In some cases, indicated in the text, samples where stabilized heat-treating at 500°C, prior and after sulphidation in oxygen and inert atmosphere, respectively. Samples

were coded according to its silica matrix precursor and Cd^{2+} content. Thus, TM*x* indicates that TMOS was used as matrix precursor, *x* being the nominal particles wt%, referred to SiO_2, if the whole Cd^{2+} forms CdS. The prefix TE is used in the cases the matrix was prepared from TEOS.

2.2. *Nitrogen Fisisorption*

The composites were texturally characterized by isothermal nitrogen adsorption in an automatic device, Sorptomatic 1990 (Carlo Erba). Prior to the experiment, samples were degassed at 100°C, under a rotative vacuum pressure. The isotherms have been developed until nitrogen saturation pressure when the adsorption saturation is reached. At this point, the desorption equilibrium branch is obtained until a relative equilibrium pressure of 0.12. Samples specific surface area and pore volume have been estimated by the BET method and the nitrogen adsorbed volume at saturation, respectively. In order to calculate the pore size distributions Horvath-Kawazoe method [35] and Baret-Joyner-Halenda (B.J.H.) method [36] have been employed for adsorption and desorption branches, respectively.

2.3. *X-Ray Absorption Spectroscopy*

XAS experiments were carried out on the beam line XAS3 at D.C.I. storage ring (Orsay, France) with an electron beam energy of 1.85 GeV and an average current of 250 mA. Data were collected with a fixed exit monochromator using two flat Si (311) crystals in transmission modes. Detection was made using two ion chambers with air as filled gas and a photomultiplier with a scintillation plastic for the fluorescence yield detection. The fast-EXAFS-acquisition operative mode [37] was used to collect at least ten spectra in a limited time with sufficient signal-to-noise ratio. Energy resolution was estimated to be about 2 eV from the Cu foil 3D near-edge feature. The energy calibration was monitored using the Cu foil sample and was set at 8991 eV at the first maximum of the derivative spectrum. EXAFS spectra were performed over a range of 1000 eV above the Cd edge.

A conventional procedure [38] has been used to analyze the EXAFS spectrum at a given X-ray energy E, $\chi(k)$, where $k = [\frac{8\pi^2 m_e}{h^2}(E - E_0)]^{1/2}$ is the photoelectron wave vector modulus, m_e being the electron mass, E_0 the threshold energy, and h the Planck's constant. As usual, an approximate energy value near the edge (E_{0i}) was initially assigned to $k = 0$. Then, during fitting, $\Delta E_0 = E_0 - E_{0i}$ is treated as an additional parameter.

To evaluate the neighbor's position around the absorber atoms, the well-known theoretical EXAFS function was used [38]:

$$\chi(k) = \sum_j \frac{N_j}{R_j} \exp\left(-2k^2\sigma_j^2\right)\exp\left(\frac{\Gamma_j R_j}{k}\right) \times f_j \sin[2kR_j + \varphi_j(k)]. \quad (1)$$

This expression describes the EXAFS oscillations for a Gaussian distribution of neighbors around the absorber atom, in the single scattering theory and in the plane-wave approximation. N_j is the average coordination number for the Gaussian distribution of distances centered at R_j. σ_j is the Debye-Waller contribution, $\varphi_j = 2\delta(k) + \gamma_j(k)$ is the phase shift, $\delta(k)$ and $\gamma_j(k)$ being, respectively, those of the central and backscattering atoms. f_j is the amplitude of the backscattering atoms, $\Gamma_j = k/\Lambda(k)$, $\Lambda(k)$ being the photoelectron mean free path.

The Fourier Transform (FT) of $k^3\chi(k)$ is the Pseudo Radial Distribution Function (PRDF). This transform is related to the radial distribution of atoms surrounding the Cd atoms with a shift caused by the scattering phase [39]. $f_j(k)$ and $\varphi_j(k)$ have been theoretically calculated by the method reported by Rehr et al. [40]. To avoid spurious oscillations FT were calculated with a Hanning window selecting the transform range above the edge indicated in Table 1.

The X-ray absorption near edge structure (XANES) spectra were normalized by first subtracting a Victoreen law, extrapolated from the low-energy region, and then the results were multiplied by a scale factor. Only qualitative interpretations based in some currently accepted empirical notions are presented here.

In our data-fitting procedure we used the FEFF program [40] which include a calculation of $\Lambda(k)$, to calculate the scattering amplitudes and phase-shift functions. This program could give an underestimation of the number of coordination, N_{CN}. To elude this drawback, we began fitting the first peaks of the CdO and CdS references with assumption of Cd─O (6×2.30 Å) and CdS (4×2.62 Å) coordination numbers from the Shannon's table of ionic radii [41]. As these coordination do not work, N_{CN} was fixed at a reasonable integer to obtain a rough fitting, and then small variations of σ_1 and R_1 were allowed to obtain the best fitting. Finally,

Table 1. EXAFS result of Cd K-edge for TM and TE composites.

Edge	Sample	ΔR (Å)	Δk (Å^{-1})	Bonding	N_{CN}	R (Å)	σ^2 (Å^2)	ΔE_0 (eV)	ε^*(%)
26633.04	TM1	1.4–2.2	3.3–11.3	Cd–O	4.2	2.34	0.0000	−3.46	32.6
				Cd–S	1.1	2.55			
26629.81	TM5	1.2–2.5	3.4–11.4	Cd–O	2.7	2.35	0.0025	−10.48	3.8
				Cd–S	1.1	2.50			
26629.81	TM10	1.5–2.6	3.6–12.0	Cd–O	1.3	2.28	0.0006	−12.60	8.3
				Cd–S	2.2	2.54			
26628.19	TE1	1.2–2.7	3.4–12.0	Cd–O	2.7	2.21	0.0004	−5.26	61.9
				Cd–S	1.6	2.47			
26628.19	TE5	1.2–2.5	3.3–13.0	Cd–O	2.4	2.24	0.0007	−6.65	21.0
				Cd–S	1.6	2.49			
26629.81	TE10	1.5–2.5	3.5–11.5	Cd–O	4.9	2.43	0.0003	−16.6	39.5
				Cd–S	0.4	2.61			
26626.57	CdO	1.2–2.4	3.5–12.5	Cd–O	6	2.49	0.0005	−15.74	38.9
26626.57	CdO	2.5–3.7	3.5–12.5	Cd–Cd	12	3.33	0.0005	−6.5	81.7
26634.66	CdS	1.6–2.8	3.6–12.0	Cd–S	4	2.53	0.0003	−8.0	30.7

$^*\varepsilon = \sum(k^3\chi(k)_{exp} - k^3\chi(k)_{calc})^2 / \sum(k^3\chi(k)_{exp})^2$.

a fine fitting of N_{CN} is carried out. For analysis of Cd-Cd scattering in CdO, we have taken 12 as initial coordination number and 3.33 Å as next nearest neighbors distance. The distances resulting from the fitting agree very accurately with the actual crystallographic data of these compounds. The N_{CN} resulting from the fitting are used to fix a scale factor of 0.45–0.50 for the FEFF program.

The first peak positions of radial distributions of Cd K-edge of TM and TE samples, except for TM10, are consistent with a major content of CdO. However, they seem too broad to be regarded as single shells. Since a single bond distance did not give a good fit of the filtered nearest neighbor $k^3\chi(k)$ signals, a two-shell model was introduced. We began getting the best fit for a Cd–O single shell model. The starting values of the nearest neighbors' distance and coordination numbers were those of Cd–O in CdO. Then, we added a second shell with S. Since the interatomic distance and ΔE_0 fitting parameter are highly correlated, we first completed a fit in frequency by letting float R_1 and R_2, and ΔE_0. Then, as N_{CN} and σ^2 are also highly correlated, we usually let them to float up to obtain rough values. Finally, a finer fitting of bond distances is carried out.

3. Structural Models

In this section we summarize the main points of the approach previously reported in this Journal [32]. The pores were classified according to the particle arrangement. Type I pores are those interstices among four contacting particles. Type II pores are holes between noncontacting particles which are not large enough to contain at least one particle, otherwise, they are type III. These spheres are formed, as well, by a similar arrangement of smaller spheres of R_i radius, q_{i+1} being the radius ratio, $q_{i+1} = R_{i+1}/R_i$. These spheres could be also formed by random close packed spheres of $R_{i-1} = R_i/q_i$ radius. The model pore volume distributions, $p(K)$ were calculated from the largest sphere radius inscribed within the interstices [42] and expressed as a function of a reduced variable K ($K = r/R$, r being the pore radius and R the particle radius). In this way, the results can be extrapolated to whatever particle size. K at the ith level, K^i, is related to the pore size, r^i, and elementary particle size, R_0, by the relationship

$$K^i = \frac{r^i}{R_i} = \frac{r^i}{\prod_1^i q_i R_0} \tag{2}$$

The models are assisted to converge toward a particular structure introducing random voids into the structure [43] and relaxing the network applying the Lennard-Jones potential [44]. We have created a catalog of pore size distributions and compared their volume distribution derivatives $\psi(K) = K^2 p(K)$, traced as a function of $\log K$, to that of a series of gels (measured by means of N_2 adsorption method) to choose the more appropriate model. The distribution of minimum energy is found by a Monte Carlo algorithm.

The models are identified according the following nomenclature: X Py Lz

X indicates the type of the three basic spherical models, H, D and S, defined by the closeness of contact conditions. Their compactness grows from H to S.
y is the percentage of added porosity
$z = 10 \cdot \sigma$ parameter Lennard-Jones potential, i.e., L8 means $s = 0.8$. LJ indicates a nonrelaxed model.

We use the calculated value $K_{\max}$ as a criterion to choose the more appropriate model from our catalog. Data on the pore volumes associated with different hierarchical levels (e.g., micro-, meso-, or macropores), size of aggregates, the local density of the ith aggregation level, and packing of the successive levels can be obtained.

4. Results and Discussion

The first derivatives of the normalized XANES spectra are represented in Fig. 1. There is a slight edge shift toward higher energies between the CdO and CdS spectra. This is consistent with the notion of a stronger covalency of CdO bond. In the case of the composites under study, it is not immediate to infer any consequence because the edge position has to be influenced by the small size of the crystallites. More discriminating differences can be obtained from a shape analysis. The edge width and oscillation amplitude are features commonly associated to the covalent character of the probe-backscatterer atoms bond. It can be used to determine the width of the valence band which is a measure of splitting of the degenerate energy and an indication of the absorber symmetry [45, 46]. The wider is the edge and the lower are the oscillation amplitudes the higher is the covalent character of this bond and, therefore, lower the coordination. Therefore, compounds such as CdO [47] with highly symmetric coordination has a small edge width. The edge width, which is commonly defined as the full width at half maximum of the main peak in the first derivative, decreases from TM to TE spectra. In the case of TE samples, the edge width decrease with increasing Cd concentration, contrary to TM spectra in which TM10 presents the widest edge, indicating a low coordination of Cd. Conversely, the edge width should be large for highly distorted coordination as in CdS [48] which at room temperature presents a distorted blende-type tetrahedral coordination of Cd. The oscillations are wider in CdO than CdS commercial powdered crystals used as reference as corresponds to their respective coordination symmetry. We interpret edge width and oscillation amplitudes as an indication of the actual CdS content. TM10 and TE1 are the samples having the XANES derivative more similar to CdS one.

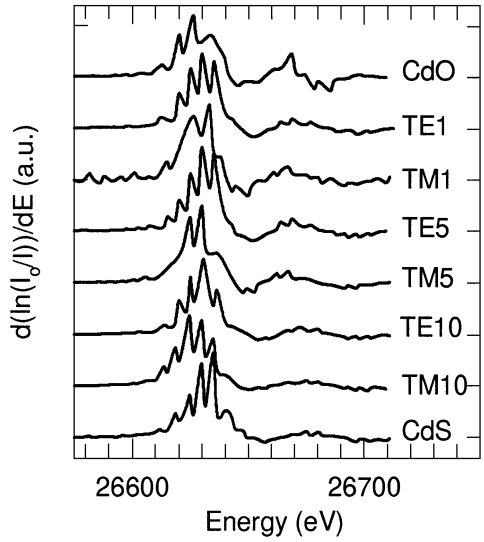

Figure 1. First derivative of XANES spectra at room temperature of Cd K-edge for TM and TE composites beside CdO and CdS commercial powdered crystals used as references.

Different local order around Cd atoms in gels regarding the bulk CdO and CdS are immediately inferred from the shape, amplitude and frequency of the EXAFS spectra Cd K-edges, shown in Fig. 2. The oscillations are smaller and vanish at lower energies than pure CdS and CdO because of the small size of crystallites. The high coordination symmetry of pure CdO is illustrated by the Fourier Transform of the $k^3\chi(k)$ signals (Fig. 3). The arrangement is ordered enough to observe the second peak corresponding to Cd—Cd distances, contrary to CdS in which only Cd—S is observable. Between the signals of the composites, the TM10 clearly differs from the rest especially because the peak position.

The fits obtained in the real space are represented in Figs. 4 and 5. The exploitation of the nonlinear behavior needs to design a strategy to avoid the CdS domains growth with concentration. Table 1 lists the values used in Fourier filtering and the structural data resulting from the fitting.

Contrary to what happens in TM samples, the number of O as nearest neighbors increase from low to high

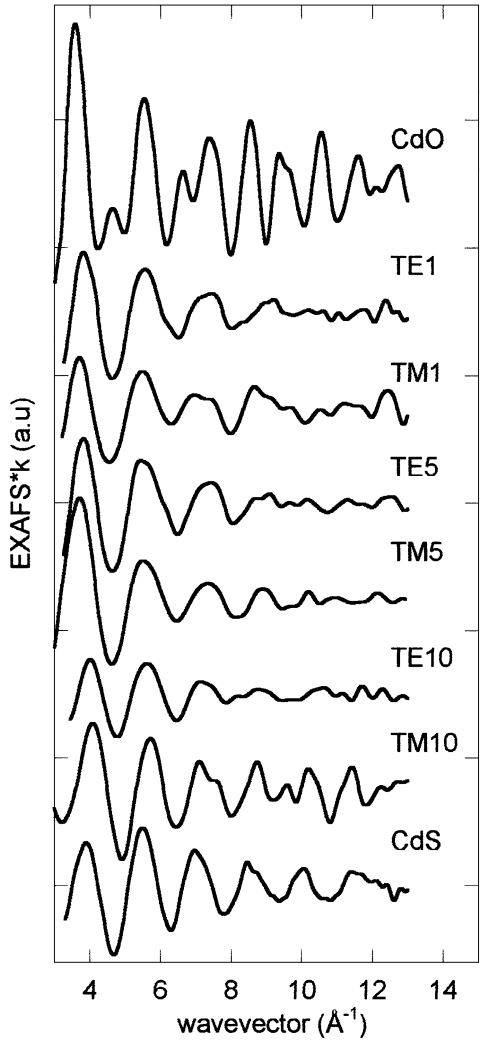

Figure 2. Room temperature EXAFS spectra of Cd $k\chi(k)$ weighted signals for TM and TE composites beside CdO and CdS commercial powdered crystals used as references.

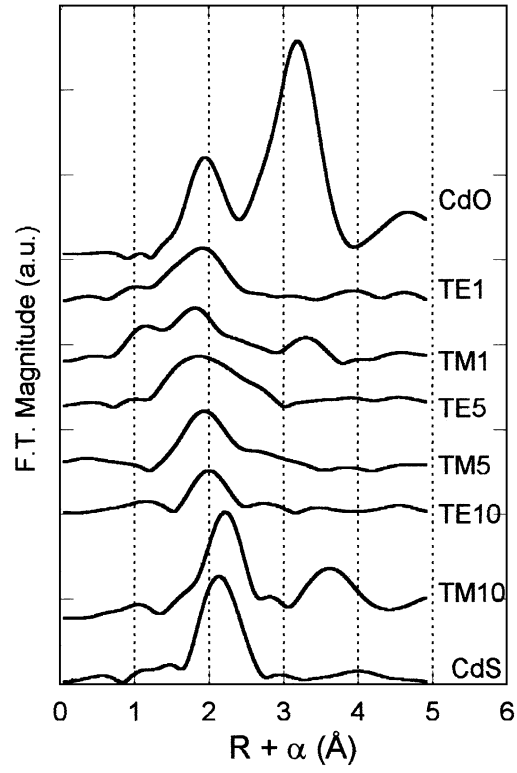

Figure 3. Fourier transforms of Cd $k^3\chi(k)$ weighted signals for TM and TE composites beside CdO and CdS commercial powdered crystals used as references. Vertical grids are shown as a eye-guide.

Cd concentration in TE samples. The bond distances differ in no more than 2% from the standard values of the reference materials. The crystallites have a high surface-to-volume ratio that can cause distortion, although it is not plausible to think that there are CdS and CdO nanocrystallites existing separately. This is a distortion that reasonably corresponds to a situation in which O and S share positions as Cd nearest neighbors.

The shapes of nitrogen adsorption isotherms can be associated to Type IV isotherms, according to IUPAC classification [49]. They present the characteristic hysteresis loop, which is associated with capillary condensation taking place in mesopores, and the limiting uptake over a range of high P/P_0. The analysis of the isotherm allows to obtain samples textural characteristics as their specific surface and pore volume, which are given in Table 2. The values show an important S_{BET} and V_p increase referred to the TM0 sample due to the effect of the precursor salt in the gelling process [29]. The addition of a salt in the sol stage induces an increase in the resulting gel porosity. For an amount of salt higher than in TM1, this effect is less important than the decrease in the textural parameters caused by the increase of nanocrystals amount in the composite pore network. From a CdS content of 5 wt%, S_{BET} evolves up to reach values lower than in TM0. The pore volume decreases with CdS content and becomes equal to TM0 in TM10.

Pore size distributions obtained from desorption branches by means of B.J.H. method [36] are represented in Fig. 6. The desorption branch features the external pore structure. For increasing CdS concentration, there is a regular shift of the distribution maxima to lower mean pore radius as well as a decrease of the contribution of larger pores to the total porous

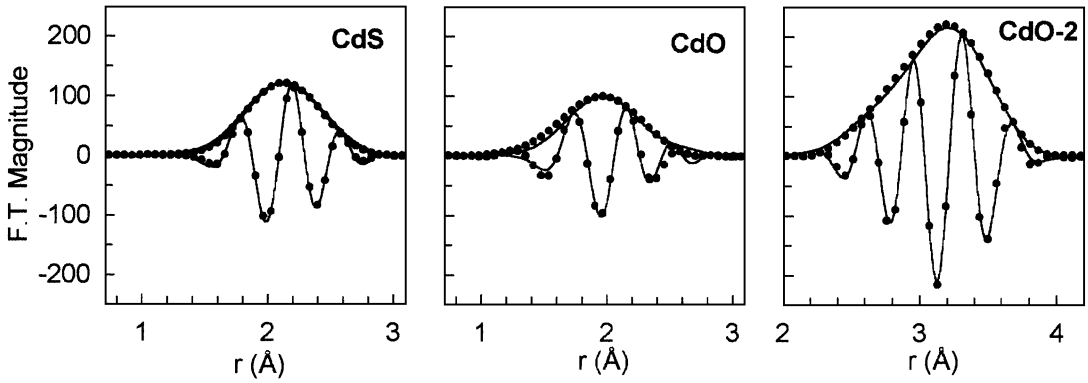

Figure 4. Comparison of experimental (points) with calculated (continuous line) modulus and imaginary part of the filtered EXAFS data in R-space at Cd K-edge for Cd–O and Cd–Cd shells, and Cd–S shell of CdO and CdS commercial powders, respectively.

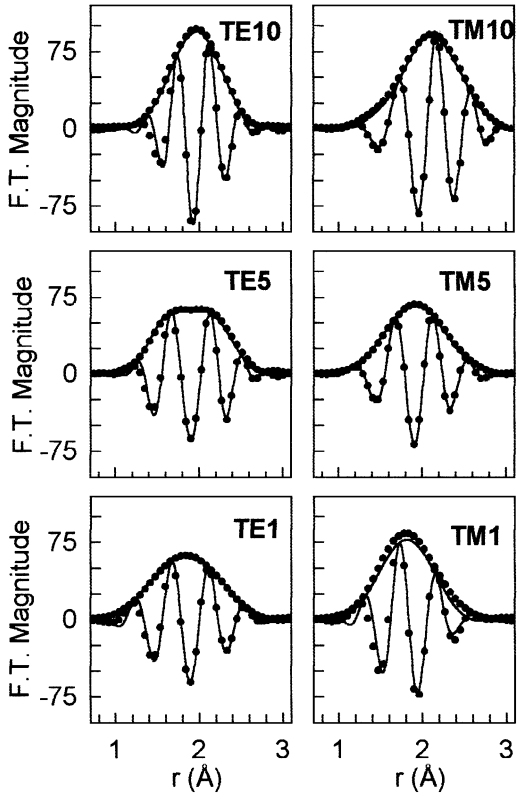

Figure 5. Comparison of experimental (points) with calculated (continuous line) modulus and imaginary part of the filtered EXAFS data in R-space at Cd K-edge for the nearest neighbors shell of TM and TE composites.

volume. However, this does not imply necessarily, as can be thought in a simple analysis, that large pores are filled prior to small ones but the evolution needs a more elaborated interpretation. We consider that SAXS results of TM composites are fitted by a nanocrystalline shell model [50]. According to this idea, if a CdS layer

Table 2. Data resulting from N_2 isotherms analysis.

Sample	S_{BET} ($m^2 \cdot g^{-1}$)	V_p ($cm^3 \cdot g^{-1}$)
TM0	458	0.42
TM1	624	1.00
TM3	505	0.74
TM5	387	0.72
TM10	364	0.42

grows on the wall of a r_1 radius pore, this has to be thinner than in a r_2 pore ($r_1 < r_2$) because of their lower V/S ratio (Fig. 6). The layers in such a sample (with an established Cd content, homogeneously distributed throughout the sample) are thicker in r_2 pores because they have less relative surface to grow. Thus, the mean pore size becomes smaller and the pore size distribution increasingly uniform when CdS concentration increases. Accordingly, from a first inspection of pore volume obtained from adsorption branch it can be concluded that micropores collapse and mesopores reduce their size for increasing CdS concentration.

We have applied our models to the volume distributions obtained from B.E.T. adsorption branch of TM10 and TM1 samples. The BET experiment resolves two mesopore levels for both TM1 and TM10 (Fig. 7). However, it can only tell the upper limit ($r_t^0 = K_t^0 R_0$) of the pore in aggregates of the elementary particles (dotted lines in Fig. 7) overlapped with the smallest pores of the first-level distribution. Overlapping means that the particles can be perfectly fitted together, letting at the i-level type III pores between them which are type II at the $(i+1)$-level.

Structural parameters of these distributions can be calculated from the analysis of the distributions.

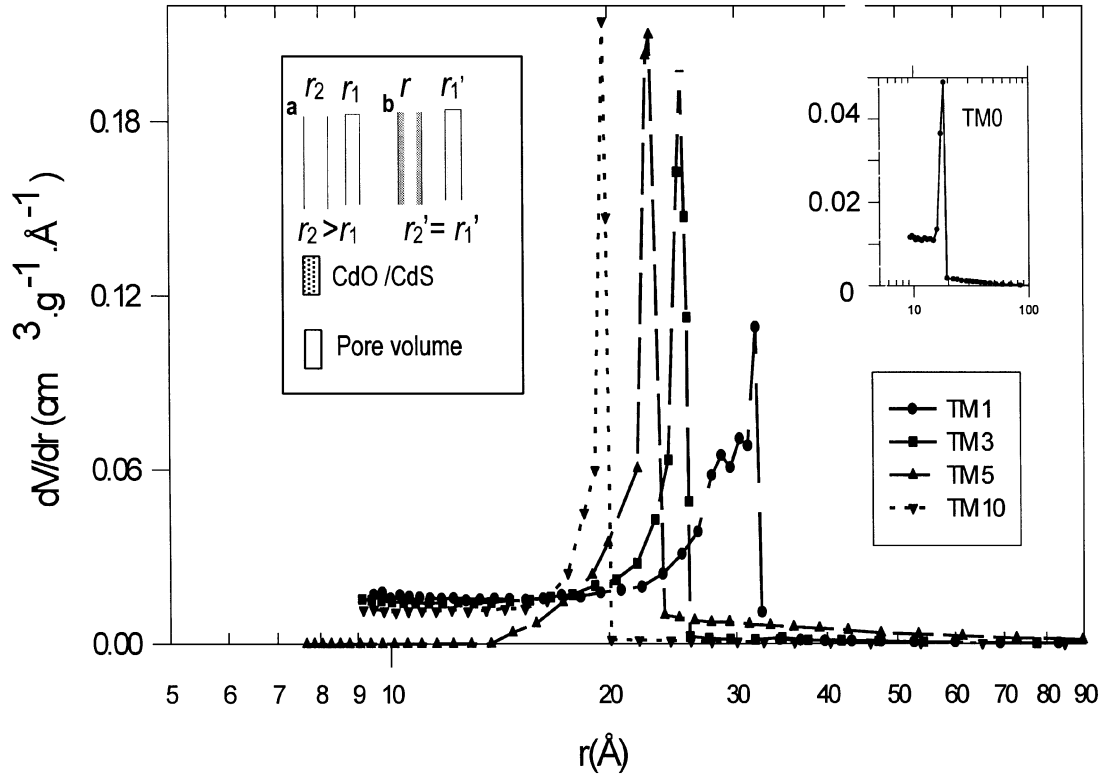

Figure 6. Pore size distributions obtained from desorption branches employing the B.J.H. method [51]. The inset sketches the influence of the pore size in crystal size (see text).

Suitable fitting for the TM1 pore volumes distribution was accomplished applying models as loose as DP20L9 and HP20LJ to describe levels 1 and 2, respectively. The distribution presents a long tail that indicates type III pores at the upper level. According to these models we have obtained the structural parameters abridged in Table 3. When $R_2/R_1 > 3$, as it occurs in TM1, we ought to think in loose models to which porosity has been added. The HP0L8 and HP0LJ of our catalogue fit adequately the pore volume distribution of TM10 the structure. If sample R_2/R_1 is near 3, then we have to consider hexagonal packing of aggregates. These results are materialized in Fig. 8.

Under the hypothesis of a spherical shell nanocrystallites model, the CdS shell in TM10 is thicker than in TM1. In this manner, there is less micropores the distribution of mesopores shifts by approximately 2 nm toward smaller sizes. This result agrees with our XAS finding. The V_{CdS}/V_{CdO} ratio (being V_{CdS} and V_{CdO}, respectively, the volume occupied by CdS and CdO in a particle) monotonely increases with particle radius. Prior to H_2S gas diffusion, CdO particles in TM1 are smaller than in TM10. Diffusion causes formation of smaller CdS entities in TM1 than in TM10 with favorable conditions to present quantum confinement. However, they are in such a low concentration that the global effect is weak. On the contrary, H_2S diffusion in TM10 results in a high concentration of CdS domains but too large to behave satisfactorily. In this sense, the photoluminescence (PL) yield of quantum dots intrinsic band spectra of TM samples, stabilized with a heat treatment at 500°C, corroborate the more efficient quantum

Table 3. Calculated structural parameters for TM1 and TM10 composites.

Sample	Aggr. level	Model	K_{max}	R_i (Å)	q_i
TM1	0	—	—	12	—
	1	DP0L9	0.32	42	3.5
	2	HP20LJ	0.36	133	3.2
TM10	0	—	—	14	—
	1	HP0LJ	0.34	40	2.9
	2	HP0L8	0.26	120	3.0

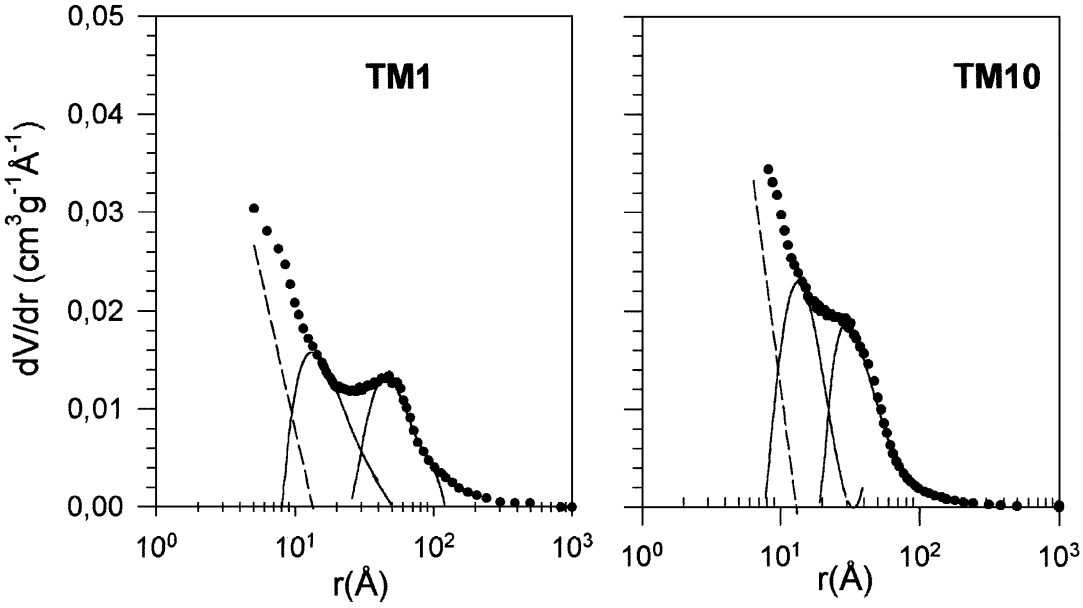

Figure 7. Interpretation of the pore size distributions.

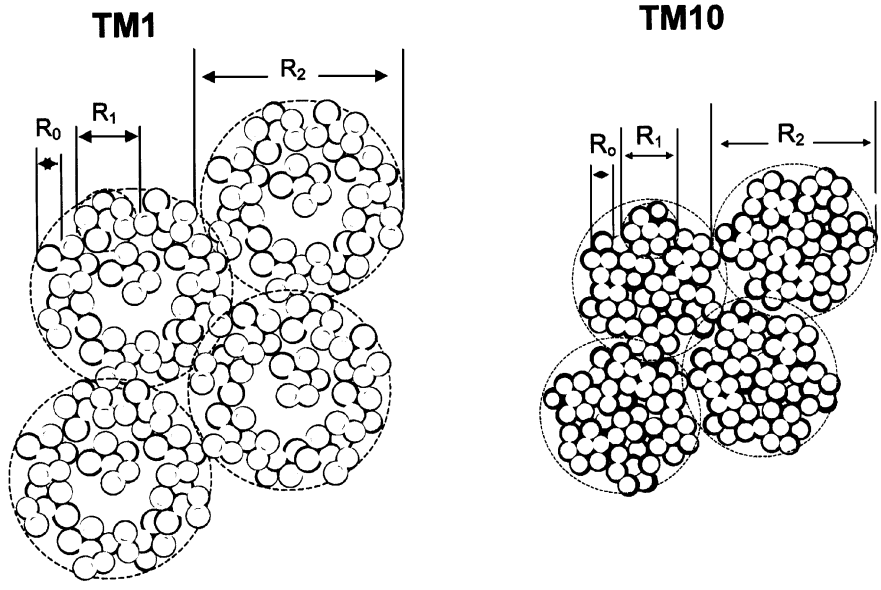

Figure 8. A schematic representation of the structures of TM1 (left) and TM10 (right) composites.

confinements in CdS dots in TM1 sample. This is evidenced by the less blue shifted intrinsic band as well as the line broadening observed in the sample with a 10 wt% of CdS (Fig. 9). Measurements in progress seem to show a superlinear increase of the integrated luminescence with the excitation intensity at room temperature. This behavior would corroborate a biexcitonic gain which is characteristic of efficient CdS Q-particles in the composite.

5. Conclusions

1. The relative amount of formed CdS crystals depends on the precursor. Contrary to what is observed when

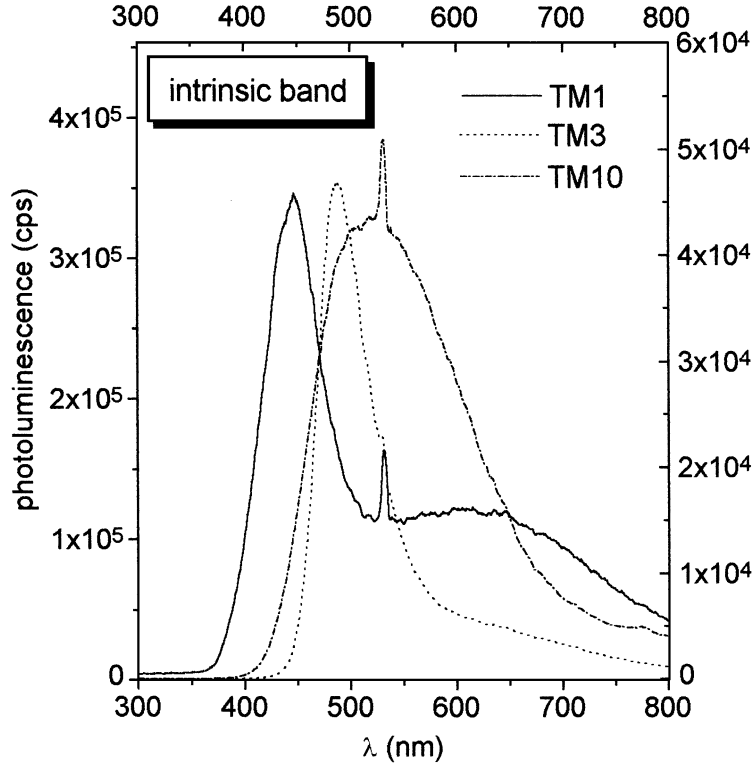

Figure 9. PL yield of the TM samples quantum dots intrinsic band. PL steady-state of the intensity spectra was measured with the third harmonic of a Q-switch Nd: YAG (355 nm) laser (6 ns pulses at 10 Hz repetition rate). The laser beam was focused on the sample in a narrow rectangular stripe ($60 \times 320\,\mu m$) and the PL signal was collected in the perpendicular direction of the laser beam. The traps band signal from the CdS nanocrystals was cut with a BG-14 (Schott) color filter [52].

TEOS is used as a precursor of the silica matrix, using TMOS the relative amount of formed CdS increases with its nominal content.

2. The difference between the Cd—O and Cd—S bond lengths in these composites and the ones in the reference materials is not higher than 2% of the standards. It is plausible to think that this distortion that corresponds to a structure in which O and S share positions as Cd nearest neighbors.
3. The results on porosity are coherent with a model consisting of CdS layers that grow on the CdO particles situated at the pore walls. This layer is thicker in large pores than in small pores, reducing the size of meso- and macropores and causing collapse of micropores.
4. The CdS concentration increase leads to smaller pores a more uniform pore size distribution. The CdS crystal size in low nominal content composites has more favorable conditions to present quantum confinement but their concentration is low to present collectively a strong effect.
5. Increasing the CdS concentration results in CdS domains growth.
6. The exploitation of the nonlinear behavior needs to design a strategy to avoid the CdS domains growth with concentration.

Acknowledgment

The authors thank the Comisión Interministerial de Ciencia y Tecnología (Proyecto MAT95-0040-C02-02) and Junta de Andalucía (TEP 0015) for the financial support of this work.

References

1. R.K. Jain and R.C. Lind, J. Opt. Soc. Am. **73**, 647 (1983).
2. E.J.A. Pope and J. Mackenzie, Mater. Res. Soc. Bull. **17**, 29 (1987).
3. R. Litrán, E. Blanco, M. Ramírez-del-Solar, A. Hierro, M.A. Díaz-García, A. García-Cabañanes, and F. Agulló-López, Synth. Metals **83**, 173 (1996).

4. N. Nogami and K. Nagasaka, J. Non-Cryst. Solids **122**, 101 (1990).
5. M. Piñero, R. Litrán, C. Fernández-Lorenzo, E. Blanco, M. Ramírez-del-Solar, N. de la Rosa-Fox, L. Esquivias, A. Craievich, and J. Zarzycki, J. Sol-Gel Sci. Tech. **2**, 689 (1994).
6. N. Toghe, M. Asuka, and T. Minami, J. Non-Cryst. Solids **147/148**, 631(1992).
7. M. Guglielmi, A. Martucci, G.C. Righini, and S. Pelli, SPIE, Sol-Gel Optics III **1188**, 174 (1994).
8. T. Rajh, M.I. Vucemilovic, N.M. Dimitrijevic, O.I. Micic, and A.J. Nozik, Chem. Phys. Lett. **143**(3), 305 (1988).
9. L. Spanhel, E. Arpac, and H. Schmidt, J. Non-Cryst. Solids **147/148**, 657 (1992).
10. H. Schmidt, J. Sol-Gel Sci. Tech. **1**(3), 217 (1994).
11. L. Spanhel, H. Schmidt, A. Uhrig, and C. Klingshrirn, Mat. Res. Soc. Symp. Proc. **272**, 53 (1992).
12. M. Menning and H. Schmidt, J. Sol-Gel Sci. Tech. **8**, 1035 (1997).
13. N. Tohge, M. Asuka, and T. Minami, SPIE Proc., Sol-Gel Optics I **1328**, 125 (1990).
14. M. Nogami and K. Nagasaka, J. Non-Cryst. Solids **147/148**, 331 (1992).
15. T. Gacoin, C. Train, F. Chaput, J.P. Boilot, P. Aubert, M. Gandais, Y. Wang, and A. Lecomte, SPIE Proc., Sol-Gel Optics II **1758**, 565 (1992).
16. M. Nogami and K. Nagasaka, J. Non-Cryst. Solids **163**, 242 (1993).
17. C.H. Sing, Y. Xu, J.D. Mackenzie, J. Chee, and J.M. Liu, SPIE Proc., Sol-Gel Optics II **1758**, 485 (1992).
18. M. Tarasevich, Cer. Bull. **63**, 500 (1984) (Abstract only).
19. J. Zarzycki, Heterogeneous Chemistry Reviews **1**, 243 (1994).
20. N. de la Rosa-Fox, L. Esquivias, and J. Zarzycki, Diffusion and Defect Data **53–54**, 363 (1987).
21. N. de la Rosa-Fox, L. Esquivias, and J. Zarzycki, Rev. Phys. Appliquée **24**, C4-223 (1989).
22. M. Ramírez del Solar, N. de la Rosa-Fox, L. Esquivias, and J. Zarzycki, J. Non-Cryst. Solids **121**, 84 (1990).
23. N. de la Rosa-Fox, L. Esquivias, and J. Zarzycki, J. Non-Cryst. Solids **121**, 84 (1990).
24. M. Ramírez-del-Solar, N. de la Rosa-Fox, L. Esquivias, and J. Zarzycki, J. Non-Cryst. Solids **121**, 40, (1990).
25. N. de la Rosa-Fox, L. Esquivias, and J. Zarzycki, J. Mat. Sci. Lett. **10**, 1237 (1991).
26. E. Blanco, N. de la Rosa-Fox, L. Esquivias, and A. Craievich, J. Non-Cryst. Solids **147/148**, 296 (1992).
27. J. Zarzycki, in *Ultrastructure Processing of Advanced Materials*, *Sonogels-Development and perpectives*, edited by D.R. Ulhmann and D.R. Ulrich (Wiley, NY, 1992), p. 135.
28. C. Bagnall and J. Zarzycki, SPIE Proc., Sol-Gel Optics I **1328**, 108 (1990).
29. T. Murakata, S. Sato, T. Ohgawara, T. Watanabe, and T. Suzuki, J. Mat. Sci. **27**, 1567 (1992).
30. M. Yamane, T. Takada, J.D. Mackenzie, and Ch. Li, SPIE Sol-Gel Optics II **1758**, 577 (1992).
31. R. Litrán, R. Alcántara, E. Blanco, and M. Ramírez-del-Solar, J. Sol-Gel Sci. Tech. **8**, 275 (1997).
32. J. Rodríguez-Ortega and L. Esquivias, J. Sol-Gel Sci. Tech. **8**, (1997).
33. J. Zarzycki, in *Chemical Processing of Advanced Materials*, edited by L.L. Hench and J.K. West (John Wiley & Sons, New York, 1992), p. 84.
34. J. Zarzycki, J. Non-Cryst. Solids **147/148**, 176 (1992).
35. G. Horvath and K. Kawazoe, J. Chem. Eng. of Japan **16**(6), 470 (1983).
36. E.P. Baret, L.G. Joyner, and P.P. Halenda, J. Am. Chem. Soc. **73**, 373 (1951).
37. C. Prieto, P. Lagarde, H. Dexpert, V. Briois, F. Villain, and M. Verdaguer, Meas. Sci. Tech. **3**, 325 (1992).
38. K. Teo, *Inorganic Chemistry Concepts 9* (Springer Verlag, Berlin, 1986).
39. A.G. Mckale, B.W. Veal, A.P. Paulikas, S.K. Chan, and G.S. Knapp, J. Am. Chem. Soc. **110**, 3763 (1986).
40. J.J. Rehr, J. Mustre de Leon, S.I. Zabinsky, and R.C. Albers, J. Am. Chem. Soc. **113**, 751 (1976).
41. R.D. Shannon, Acta Crystallogr. **A 32**, 751 (1976).
42. H. Frost, ONR Technical Report No. 6 (Division of Applied Sciences, Harvard Univ., Cambridge, MA, 1978).
43. J.D. Bernal and S.V. King, Discuss. Faraday Soc. **43**, 60 (1967).
44. J.L. Finney and J. Wallace, J. Non-Cryst. Solids **43**, 165 (1981).
45. U.C. Sritava and H.L. Nigam, Coord. Chem. Rev. **9**, 275 (1973).
46. J.C.J. Bart, Adv. Catal. **34**, 203 (1986).
47. Swanson and Fuyat, NBS Circular 539, **3**, 27 (1953).
48. Osugi et al., Rev. Phys. Chem. Japan **36**, 59 (1966).
49. K.S.W. Sing et al., Pure and Appl. Chem. **57**(4), 503 (1985).
50. N. de la Rosa-Fox and A. Craievich, to be published.
51. E.P. Barret, L.G. Joyner, and P.P. Halenda, J. Amer. Chemistry Soc. **73**, 373 (1951).
52. This experiment was carried out at the Optical Science Center (Prof. Peyghambarian Group), University of Arizona, Tucson, AZ, USA.